The role of neurofilament transport in the radial growth of myelinated axons

Rawan M. Nowier[a], Anika Friedman[a,†], Anthony Brown[b,*], and Peter Jung[a,*]
[a]Department of Physics and Astronomy and Quantitative Biology Institute, Ohio University, Athens, OH 45701;
[b]Department of Neuroscience, Ohio State University, Columbus, OH 43210

ABSTRACT **The cross-sectional area of myelinated axons increases greatly during postnatal development in mammals and is an important influence on axonal conduction velocity. This radial growth is driven primarily by an accumulation of neurofilaments, which are cytoskeletal polymers that serve a space-filling function in axons. Neurofilaments are assembled in the neuronal cell body and transported into axons along microtubule tracks. The maturation of myelinated axons is accompanied by an increase in neurofilament gene expression and a decrease in neurofilament transport velocity, but the relative contributions of these processes to the radial growth are not known. Here, we address this question by computational modeling of the radial growth of myelinated motor axons during postnatal development in rats. We show that a single model can explain the radial growth of these axons in a manner consistent with published data on axon caliber, neurofilament and microtubule densities, and neurofilament transport kinetics in vivo. We find that the increase in the cross-sectional area of these axons is driven primarily by an increase in the influx of neurofilaments at early times and by a slowing of neurofilament transport at later times. We show that the slowing can be explained by a decline in the microtubule density.**

Monitoring Editor
Alex Mogilner
New York University

Received: Dec 22, 2022
Revised: Feb 8, 2023
Accepted: Feb 13, 2023

INTRODUCTION

Axon diameter is one of the basic cable properties that influence axonal conduction velocity, which is critical for neuronal function (Waxman, 1980; Hartline and Colman, 2007; Perge *et al.*, 2012; Suminaite *et al.*, 2019). In mammals, the expansion of axon caliber occurs postnatally (Matthews and Duncan, 1971; Vejsada *et al.*, 1985) and is triggered by the onset of myelination (Windebank *et al.*, 1985; de Waegh *et al.*, 1992; Hsieh *et al.*, 1994; Monsma *et al.*, 2014). Among the principal determinants of the diameter of myelinated axons in mammals and other vertebrates are neurofilaments, which are abundant space-filling cytoskeletal polymers that occupy most of the axonal volume (Cleveland *et al.*, 1991; Perrot *et al.*, 2008). Morphometric studies in mice and rats have established a direct correlation between the abundance of neurofilaments and axonal diameter (Friede and Samorajski, 1970; Friede *et al.*, 1971; Hoffman *et al.*, 1984; Nixon *et al.*, 1994). In the absence of neurofilaments, axons fail to develop normal caliber and exhibit reduced conduction velocities (Sakaguchi *et al.*, 1993; Zhu *et al.*, 1997; Perrot *et al.*, 2007).

In addition to their space-filling role, neurofilaments are also cargo of slow axonal transport that move slowly toward the nerve terminals at an average velocity on the order of millimeters per day (Lasek *et al.*, 1992; Brown, 2000, 2003, 2014). The neurofilament polymers are assembled in the cell body and then transported into and along the axons on microtubule tracks powered by microtubule motor proteins (Francis *et al.*, 2005; He *et al.*, 2005; Uchida *et al.*, 2009). The filaments move in a "stop-and-go" manner, alternating between mobile and immobile states that we have termed "on-track" and "off-track," respectively (Trivedi *et al.*, 2007). Filaments in the mobile on-track state exhibit bouts of rapid intermittent movement with brief pauses on the order of seconds in duration, occasionally switching to the immobile off-track state in which they can pause for an hour or more before moving back on-track (Wang *et al.*, 2000; Brown *et al.*, 2005; Trivedi *et al.*, 2007; Jung and Brown, 2009). Thus, the slow velocity of neurofilament transport is an

This article was published online ahead of print in MBoC in Press (http://www.molbiolcell.org/cgi/doi/10.1091/mbc.E22-12-0565) on February 22, 2023.

†Present address: Department of Chemical and Biological Engineering, University of Colorado Boulder, Boulder, CO 80309.

*Address correspondence to: Peter Jung (jungp@ohio.edu); Anthony Brown (brown.2302@osu.edu).

Abbreviations used: MT, microtubule; NF, neurofilament; NFH, neurofilament protein H; NFL, neurofilament protein L; NFM, neurofilament protein M.

average of rapid movements interrupted by pauses of various durations. The filaments move both anterogradely and retrogradely and can reverse direction, but they spend more their time moving anterogradely, resulting in a net anterograde bias (Fenn *et al.*, 2018; Boyer *et al.*, 2022).

Studies on peripheral nerve development in mice and rats have shown that the postnatal radial growth of myelinated axons is accompanied by a slowing of neurofilament transport (Hoffman *et al.*, 1983, 1984, 1985a; Watson *et al.*, 1989) and an increase in neurofilament gene expression (Lasek *et al.*, 1983; Hoffman *et al.*, 1987; Muma *et al.*, 1991). An increase in neurofilament gene expression for a given velocity is expected to result in an increase in the flux of neurofilaments into the axon from the cell body. A decrease in the neurofilament transport velocity for a given flux is expected to increase the residence time of these polymers in the axon. Thus, both the increase in gene expression and the decrease in transport velocity are expected to lead to an increase in the number of neurofilaments in the axon (Hoffman, 1995), but their relative contributions are not clear. Here, we use computational modeling in conjunction with published morphometric and kinetic data on axon caliber, neurofilament and microtubule densities, and neurofilament transport to address this question.

RESULTS

In this section, we use the computational strategy explained in *Methods* to investigate the role of neurofilament transport in the growth of axon caliber. Guided by existing morphometric data, we model neurofilament influx from the cell body over time using a simulated injection of neurofilaments at the proximal end of the axon. We confirm that the model reproduces the experimentally observed growth in axon caliber. We then use this model to simulate the kinetics of neurofilament transport and compare them with published neurofilament transport kinetics obtained by radioisotopic pulse labeling in order to validate the model and gain insight into the mechanism of neurofilament accumulation.

Morphometric analysis and model parameters

Most of the radial expansion of axons in mammals occurs after birth. Morphometric studies in rats have shown that this expansion is linear with time up to at least 5 mo of age. In Figure 1A we replot the experimental data of Hoffman *et al*. (1985a) on the average caliber of myelinated motor axons in L5 ventral roots of rats ranging from 3 to 18 wk in age. By linear regression, we obtain the relationship

$$A = 2.93\left(\frac{\mu m^2}{\text{week}}\right)t + 16.2\ \mu m^2 \qquad (1)$$

where A is the axonal cross-sectional area and t is the age measured in weeks.

As noted in the *Introduction*, it is well established that the cross-sectional area of myelinated axons in mammals is also linearly related to the number of axonal neurofilaments. However, the slope (which approximates the neurofilament density) can vary depending on the cell type and animal species (Friede and Samorajski, 1970; Friede *et al.*, 1971). In Figure 1B we replot the experimental data of Hoffman *et al.* (1984) showing neurofilament number versus axon caliber for myelinated motor axons of rat L5 ventral roots measured at 10 wk of age. By linear regression, we obtain the relationship

$$N_{NF} = \alpha_{NF}A - 88.0 \qquad (2)$$

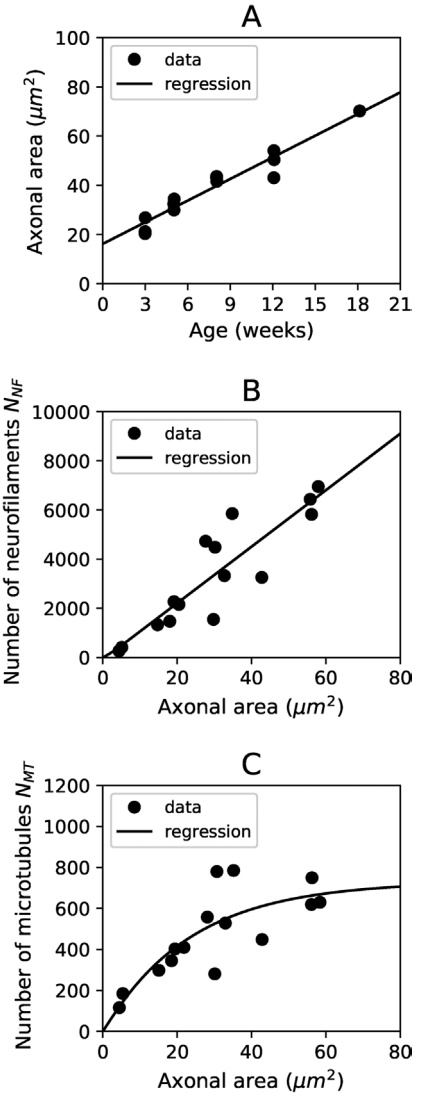

FIGURE 1: Morphometric data collected from the L5 ventral roots of rats. (A) Growth curve showing the average axonal cross-sectional areas of the largest 25% of myelinated axons from 3 to 18 wk of age. (B) Relationship between neurofilament number and axonal cross-sectional area. (C) Relationship between microtubule number and axonal cross-sectional area. To fit the data in B and C for cross-sectional areas >5 μm², we used the regressions in Eqs. 2 and 4, respectively. To extrapolate the regressions in B and C to the origin for cross-sectional areas <5 μm², we used the second-order polynomial expressions in Eqs. 3 and 5, respectively. The data in panel A are from Figure 6 in Hoffman *et al.* (1985a). The data in panels B and C are from Figure 10 in Hoffman *et al.* (1984). The points represent the experimental data. The black lines represent the regressions.

for axonal cross-sectional areas >5 μm², where N_{NF} is the number of neurofilaments in the axonal cross-section, A is the cross-sectional area measured in μm² and the slope is $\alpha_{NF} = 115/\mu m^2$. To extrapolate the regression back to the origin for axonal cross-sectional areas <5 μm², we used the polynomial regression

$$N_{NF} = \left(79.8/\mu m^2\right)A + \left(3.52/\mu m^4\right)A^2 \qquad (3)$$

For microtubules, the situation is more complicated. In Figure 1C we replot the experimental data of Hoffman *et al.* (1984) for

microtubule number versus axon caliber, also measured at 10 wk of age. While the increase in microtubule number is approximately linear for small axons, the rate of increase declines with increasing cross-sectional area, resulting in a nonlinear relationship. Thus, there is a decline in microtubule density during radial axon growth of rat motor axons. This has also been reported by Friede and Samorajski (1970) for myelinated axons in the sciatic nerves of rats and mice and by Berthold and Rydmark (1995) for myelinated axons in the ventral roots of cats. For the data in Figure 1C, we find that an exponential function fits well. By exponential regression, we obtain the following relationship:

$$N_{MT} = 731 - 736\exp\left(-\left(0.042/\mu m^2\right)A\right) \quad (4)$$

for axonal cross-sectional areas >5 μm^2, where N_{MT} is the number of microtubules in the axonal cross-section. This relationship has important implications for the transport velocity of neurofilaments. Specifically, the density of microtubules $\rho_{MT} = N_{MT}/A$ decreases with increasing cross-sectional area, resulting in a smaller on-rate and a larger diffusive search time for a neurofilament to find a microtubule track and hence, a smaller transport velocity. To extrapolate the regression back to the origin for axonal cross-sectional areas <5 μm^2, we used the polynomial regression

$$N_{MT} = \left(28.8/\mu m^2\right)A - \left(0.375/\mu m^4\right)A^2 \quad (5)$$

Note that although the morphometric relations in Eqs. 2–5 are based on measurements at one age, for the present study we assume that they apply to all ages. We believe that this is justified because studies in the sciatic nerves of young and old rats and mice have not revealed age-dependent differences in the relationship between neurofilament or microtubule density and axon caliber (Friede and Samorajski, 1970).

To simulate neurofilament transport, the directionality of the filaments was set to anterograde initially, which is required for the filaments to enter the axon. For the rate constants in the model, we used the values that were estimated for neurofilament transport in mouse ventral root and sciatic nerve by Jung and Brown (2009). The one exception was the on-rate γ_{on}, which now emerges from the microtubule density as explained in *Methods*. For the reversal rates, we assumed $\gamma_{ar} = 4.20 \times 10^{-6}\ s^{-1}$ and $\gamma_{ra} = 1.40 \times 10^{-5}\ s^{-1}$. For the off-rate, we used the value $\gamma_{off} = 4.50 \times 10^{-3}\ s^{-1}$ determined experimentally in cultured neurons using the fluorescence photoactivation pulse-escape method (Trivedi *et al.*, 2007). For the anterograde and retrograde velocities, we assumed $v_a = 0.5$ μm/s and $v_r = -0.5$ μm/s, respectively (Jung and Brown, 2009). The radial diffusion coefficient of neurofilaments on which the on-rate is directly dependent was adjusted so that the velocity of the simulated radiolabeled pulse of neurofilaments matched the initial velocity of the experimental measured radiolabeled pulse in the ventral root and sciatic nerve of 3-wk-old animals (Hoffman *et al.*, 1985a). The resulting value of $D_{NF} = 2.28 \times 10^{-6}\ \mu m^2/s$ was within an order of magnitude of the value used by Xue *et al.* (2015). For the on-track rate constants that govern the transition between on-track movements and pauses, we used values of $\gamma_{01} = 6.40 \times 10^{-2}\ s^{-1}$ and $\gamma_{10} = 1.40 \times 10^{-1}\ s^{-1}$ which were previously determined experimentally in cultured neurons using time-lapse imaging (Jung and Brown, 2009). We then adjusted these rate constants to match the peak of a Gaussian fit of the simulated pulse of radiolabeled neurofilaments to the peak of the Gaussian fit of the corresponding experimental data 15 d after radiolabeling in 3-wk-old animals. This resulted in values of $\gamma_{01} = 0.080\ s^{-1}$ and $\gamma_{10} = 0.139\ s^{-1}$ (see Figure 5 later in this article).

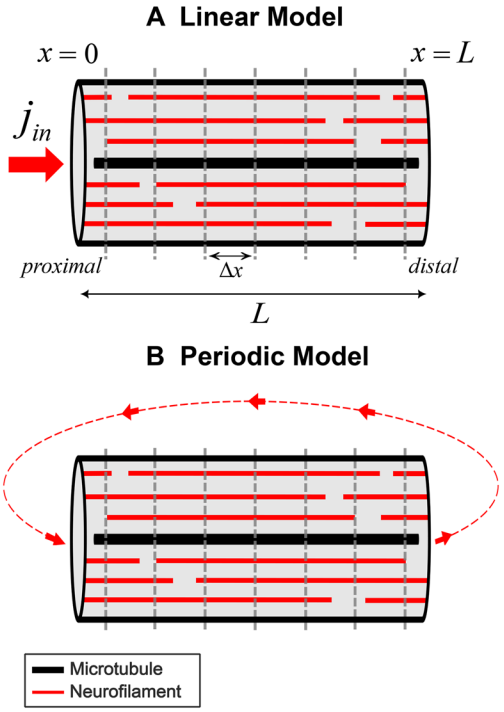

FIGURE 2: Modeling the axonal neurofilament flux. (A) The linear version of the computational model simulating neurofilament transport in a linear open axon of length *L* that is discretized to smaller bins (Δ*x*). (B) The periodic version of the computational model simulating neurofilament transport with a periodic boundary where neurofilaments move in a closed path, i.e. those that leave one end feed into the other end and vice versa. The periodic model was used to extract the influx required to achieve radial growth in the linear model.

Simulating the growth of axon caliber

Table 1 shows the average axon area and neurofilament and microtubule numbers extracted from the experimental data of Hoffman and colleagues in rat ventral roots. To quantify the contribution of gene expression to caliber growth, we first used the periodic implementation of our six-state kinetic model (Figure 2B; see *Methods*) to find the influx j_{in} (i.e., the number of neurofilaments entering the axon proximally per unit time) that is required to achieve the increase in axonal neurofilament content in these experimental data from 3 to 18 wk of age (Figure 3A). The rate of increase in the influx decreases with time and could be fitted to the following exponential function:

$$j_{in} = 21.7\,\frac{1}{s} - 10.4\,\frac{1}{s}\exp\left(-0.207\,t\right) \quad (6)$$

Age (wk)	Axonal area (μm^2)	N_{NF}	N_{MT}
3	25.0	27.8×10^2	475
5	30.8	34.5×10^2	531
8	39.6	44.6×10^2	593
12	51.4	58.1×10^2	647
18	69.0	78.3×10^2	691

The average axonal cross-sectional area, number of neurofilaments, and number of microtubules of myelinated axons of rat L5 ventral roots from 3 to 18 wk of age. Data from Figure 10 in Hoffman *et al.* (1984) and Figure 6 in Hoffman *et al.* (1985a).

TABLE 1: Morphometric measurements.

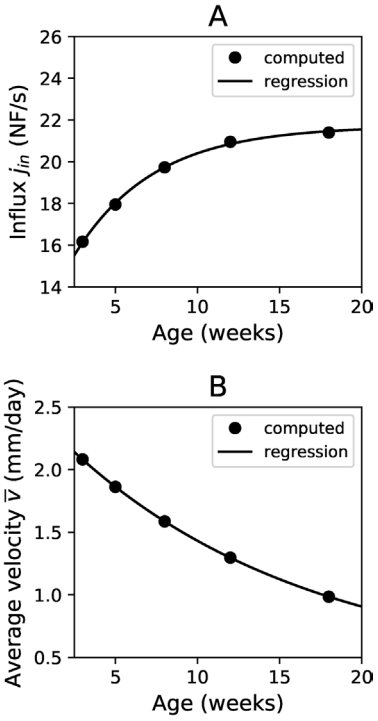

FIGURE 3: Influx and velocity vs. animal age. (A) The calculated influx in units of neurofilaments per second (NF/s) that is needed to achieve the target axonal caliber and neurofilament content shown in Table 1 for the average myelinated axon at 3, 5, 8, 12, and 18 wk of age. (B) The calculated average neurofilament transport velocity (mm/day) at the same ages. The model predicts a nonlinear increase in the neurofilament influx and a nonlinear decrease in the average velocity. The solid circles represent the calculated values, and the lines represent the exponential regressions shown in Eqs. 6 and 7.

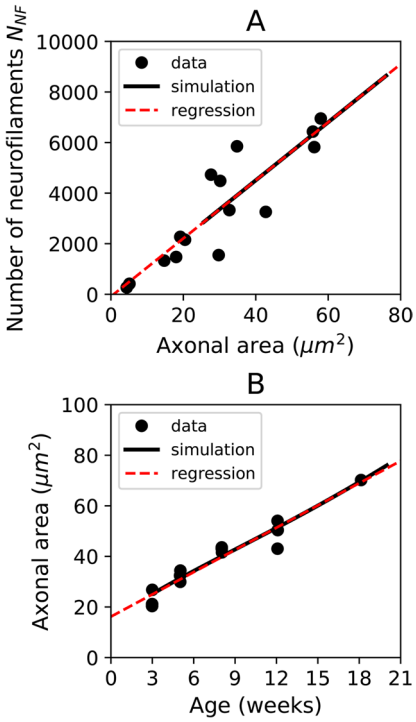

FIGURE 4: Computational simulation of the radial growth curve of myelinated axons during postnatal rat development. (A) The relationship between neurofilament number and axonal cross-sectional area generated by the model (solid black line) closely matches the regression to the experimental data (dashed red line). (B) The growth of axonal cross-sectional area with age predicted by the neurofilament accumulation in A (solid black line) starting at 3 wk closely matches the regression to the experimental data (dashed red line). The points represent the experimental data extracted from Figure 6 in Hoffman *et al.* (1985a).

where t is the time in units of weeks. The rate of neurofilament influx plateaus in older animals, similar to the plateau in microtubule density observed at larger axonal cross-sectional areas in Figure 1C.

Figure 3B shows the average velocity calculated using Eq. 26. As neurofilaments accumulate in the axons (Figure 1B) and the microtubule density declines (Figure 1C), there is a reduction in the accessibility of the neurofilaments to their microtubule tracks. This results in a decline in the average transport velocity according to the regression

$$\bar{v} = 0.368\frac{mm}{day} + 2.10\frac{mm}{day}\exp(-0.068\ t) \qquad (7)$$

Note that in our model this slowing arises not from a change in the actual velocity of movement (v_a or v_r), but rather an increase in the proportion of the time spent pausing. Later in this section, we will discuss the significance of the decline of the neurofilament velocity and the plateauing influx for the growth in axon caliber.

Having established the influx using the periodic model, we next used the linear implementation of our six-state kinetic model (Figure 2A; see *Methods*) to simulate the growth of an open 1-mm-long axon using discretized time intervals of Δt = 1 s and discretized spatial increments of Δx = 1 μm. The sequence of steps in the simulations were as follows: we started with the average numbers of neurofilaments and microtubules observed experimentally at t = 3 wk (Table 1) and distributed them uniformly along the model average axon. Then, we allowed the axon to mature in silico. At each time step Δt, we first updated the number of microtubules and the cross-sectional area according to Eqs. 1 and 4. This was done simultaneously, as the number of microtubules and the cross-sectional area are directly linked. Subsequently we recalculated γ_{on} (Eq. 29) using the updated number of microtubules and cross-sectional area. Then we injected neurofilaments into the proximal end of the axon at the rate described by Eq. 6 and updated the numbers of neurofilaments in the six kinetic states throughout the axon according to Eqs. 22, 23, and 25, allowing the filaments to cycle between these kinetic states.

Figure 4 shows that the resulting model can match the experimental data on neurofilament accumulation and radial axonal growth. Thus, the linear model can explain the rate of increase in axonal cross-sectional area in a manner consistent with the experimentally determined neurofilament and microtubule densities.

Simulating a radioisotopic pulse-labeling experiment

To validate the model, we sought to determine whether the same set of parameters used to match the growth in axon caliber in terms of the neurofilament and microtubule densities can also match the neurofilament transport kinetics. To do this, we adapted the linear model to simulate the movement of a pulse of radiolabeled neurofilaments (see *Methods*) and compared the resulting transport kinetics to experimental data obtained by radioisotopic pulse labeling in motor axons of rat lumbar ventral root and sciatic nerve (Hoffman *et al.*, 1985a). In these experiments, radioactive amino acid was injected into the lumbar spinal cord of rats in order to create a pulse of radiolabeled proteins in the cell bodies of motor neurons in the anterior horn. Animals were then killed at intervals, and the distribution of

radiolabeled NFM was analyzed over a distance of 13 cm extending from the ventral root into the distal sciatic nerve by cutting the nerve into segments, separating the proteins by electrophoresis, and quantifying the radiolabeled proteins by autoradiography (Brown, 2014). Because we lack experimental data on the caliber and neurofilament and microtubule content of motor axons along the rat sciatic nerve at the appropriate ages, we used the morphometric data obtained in the L5 ventral roots (Figure 1; Hoffman *et al.*, 1984, 1985a) and assumed that these parameters were constant along the nerve. We then simulated neurofilament transport in a 200-mm-long axon for 24 wk with a radioactive pulse initiated at either 3 or 12 wk of age.

Figure 5 shows the comparison of our simulations to the experimental data of Hoffman *et al.* (1985a). The model generates a wave that spreads as it propagates along the axons as described previously (Jung and Brown, 2009). A limitation of the radioisotopic pulse-labeling technique is that the injected animals must be killed for the analysis to be performed. Thus, each animal yields one time point. Because the injection of isotope into the anterior horn cannot be controlled exactly, the total radioactivity (area under the curves) varies considerably from animal to animal. Thus, we focused on the shape of the waves, not their amplitude. To facilitate the comparison of the wave shapes, we normalized the amplitudes of the peaks of the simulated waves to the respective waves in the experimental data. The good agreement between the wave peaks for the simulated and experimental data at 15 d after radiolabeling in 3-wk-old animals is expected because we tuned the on-track rate constants in our six-state model to achieve this (see above). However, without any further adjustment to the model parameters, we also observed good agreement of the shape of the wave at this time point and the position and shape of the waves at all other time points for both the 3- and 12-wk-old animals. This is remarkable because it means that a single set of kinetic parameters in our model captures the kinetics of neurofilaments throughout the radial growth process.

We have shown previously that the shape and spreading of the waves is dictated by the pausing and reversals of the filaments (Brown *et al.*, 2005; Jung and Brown, 2009). The simulated waves were initially sharp with a pronounced asymmetry and then assumed a more bell-shaped form over time (e.g., compare the waves at 5 d and 20 d in Figure 5A). The initial asymmetry reflects the starting conditions of our simulations. Specifically, because the neurofilaments must move anterogradely to enter the axon, we start our simulations with the radiolabeled neurofilaments all initially on-track in the anterograde motile state. As the filaments transition off-track or reverse direction, they fall behind the rest of the labeled neurofilaments, giving rise to a wave with a trailing edge. Over time, the filaments equilibrate across the kinetic states, and the wave gradually assumes a more symmetrical form. The slow rate of equilibration is a consequence of the low magnitude of the reversal and off-track rate constants.

Because our simulations using the periodic model predicted a decline in average velocity over time (Figure 3B), we also calculated the velocity of the pulse of radiolabeled neurofilaments in our simulations using the linear model for animals injected at 3 and 12 wk of age. We refer to this as the pulse velocity, which is the distance moved by the peak of the transport wave divided by the time. As observed experimentally (Hoffman *et al.*, 1983, 1985a; Watson *et al.*, 1989), the pulse velocity declined rapidly in the first week or so and then more slowly at later times. For example, the pulse velocity in the 3-wk-old animals declined from 3.8 mm/day at 5 d after radiolabeling to 2.1 mm/day at 10 d and then to 2 mm/day at 20 d (see blue symbols and line in Figure 6). However, when we calculated the average velocity of the neurofilaments at the same location in the axon in our simulations, we obtained a velocity of

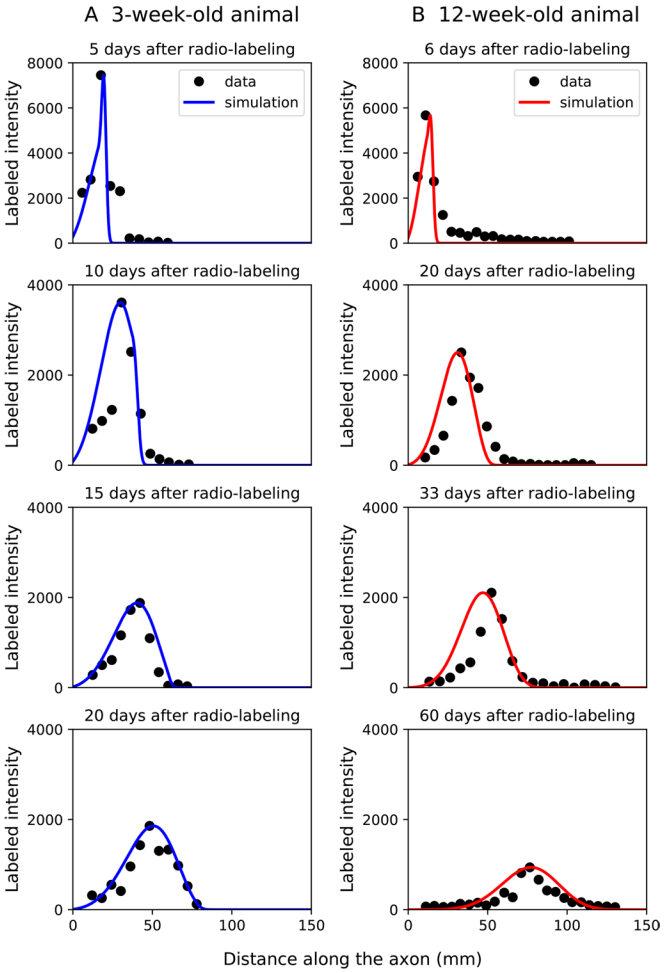

FIGURE 5: Simulation of neurofilament transport in a radioisotopic pulse-labeling experiment. The radioactivity on the *y*-axis is in arbitrary units. (A) Comparison between the simulated transport waves (blue line) and the experimental data (black data points) at 5, 10, 15, and 20 d after radiolabeling neurofilaments in 3-wk-old animals. The on-track rate constants γ_{01} and γ_{10} were tuned to match the peak of the transport wave in the model (blue line) to the mode of a Gaussian fit to the experimental data at 15 d after radiolabeling. (B) Comparison between the simulated transport waves (red line) and the experimental data (black data points) at 6, 20, 33, and 60 d after radiolabeling neurofilaments in 12-wk-old animals. To facilitate comparison of the shapes of the waves, we normalized the amplitudes of the peaks of the simulated waves to the corresponding experimental data (see text for an explanation). The black points represent the experimental data from Hoffman *et al.* (1985a).

2 mm/day at 5 d after radiolabeling at 3 wk of age, which slowed approximately linearly to 1.9 mm/day at 20 d after radiolabeling (see dashed black line in Figure 6).

This discrepancy between the velocity of the pulse-labeled neurofilaments compared with the overall neurofilament population at short times is an interesting feature of radioisotopic pulse-labeling experiments that has not previously been recognized. It arises due to the low frequency of directional reversals and the slow rate in which the nonmotile states become populated (discussed above). Two phases of slowing can be identified. Initially, the fact that the filaments all enter the axon moving anterogradely results in a net anterograde velocity that is much higher than the average for the total neurofilament population. After entering the axon, the transport

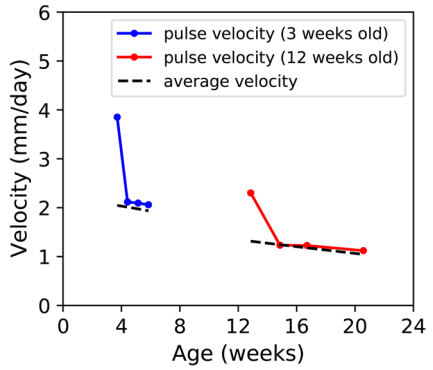

FIGURE 6: Comparison of average and pulse velocities of neurofilament transport vs. age. The pulse velocity (mm/day) was calculated over time (weeks) by tracking the peak of the simulated radiolabeled pulse in Figure 5. The pulse velocities in the animals injected at 3 wk of age (represented in blue) were measured at 5, 10, 15, and 20 d after radiolabeling, which correspond to 3.7, 4.4, 5.1, and 5.9 wk. The pulse velocities in the animals injected at 12 wk of age (represented in red) were measured at 6, 20, 33, and 60 d after radiolabeling, which correspond to 12.9, 14.9, 16.7, and 20.6 wk. The dashed black lines represent the computationally calculated average velocity of all neurofilaments at the location along the nerve corresponding to the location of the peak of the radiolabeled pulse at that time.

velocity slows as the filaments equilibrate across the long-term pausing and retrograde moving states, governed by the rate constants γ_{on}, γ_{off}, γ_{ar}, and γ_{ra}. We can estimate the equilibration time using the smallest rate constant, i.e. $\gamma_{ar} = 4.2 \times 10^{-6} s^{-1}$. The inverse of this constant, i.e. about 3 d, gives us the time for 63% of the initially labeled neurofilaments to equilibrate kinetically. By 5 d, most of the filaments had equilibrated and the actual and measured velocities had converged. Thus, the velocity of the pulse of radiolabeled neurofilaments is initially an overestimate of the true average velocity.

After the measured and actual average velocities converge, we enter a second slowing phase in which the actual average velocity continues to decline with time, but at a slower rate. This reflects the gradual decrease in the accessibility of the neurofilaments to their microtubule tracks due to the decline in microtubule density that accompanies the neurofilament accumulation. We show below that this slowing of the average neurofilament velocity contributes to the radial growth.

Contributions of flux increase and velocity slowing to caliber growth

The analyses above demonstrate that there is both an increase in the influx of neurofilaments and a decrease in their transport velocity during postnatal development of lumbar motor axons in the rat. Because both of these changes will result in an increase in the neurofilament content of the axon, both are likely to contribute to the growth of axon caliber. To quantify the relative contributions of these changes, we first formalize the relationship between the net flux j and average velocity $\bar{v}$. Because neurofilaments move bidirectionally, we must consider the net flux j, i.e. the balance between the anterograde and retrograde fluxes (see below Eq. 26), which can be expressed as

$$j = \rho_{total} \bar{v} \tag{8}$$

where ρ_{total} is the linear density of the neurofilaments in all states, i.e. $\rho_{total} = \rho_a + \rho_{a0} + \rho_{ap} + \rho_r + \rho_{r0} + \rho_{rp}$. The linear density can also be expressed as $\rho_{total} = \frac{N_{NF}}{\bar{l}}$, where $\bar{l} = l_{NF} + 1$ and l_{NF} is the average filament length. Thus, the total number of neurofilaments in an axonal cross-section is given by

$$N_{NF} = \bar{l}\,\frac{j}{\bar{v}} \tag{9}$$

The total axonal area can then be found from Eq. 2 as follows

$$A = \frac{N_{NF} + 88.0}{\alpha_{NF}} = \frac{\bar{l}}{\alpha_{NF}}\frac{j}{\bar{v}} + \frac{88.0}{\alpha_{NF}} \tag{10}$$

This expression tells us quantitatively what was intuitively clear, i.e. for a constant cross-sectional density of neurofilaments α_{NF} the axonal cross-sectional area will increase in direct proportion to the net flux of neurofilaments and in inverse proportion to the velocity.

It follows that the growth of the axonal cross-sectional area can be expressed as the increment of the axonal cross-sectional area, i.e.

$$\frac{dA}{dt} = \frac{1}{\alpha_{NF}}\frac{dN_{NF}}{dt} = \frac{\bar{l}}{\alpha_{NF}}\frac{j}{\bar{v}}\left(\frac{1}{j}\frac{dj}{dt} - \frac{1}{\bar{v}}\frac{d\bar{v}}{dt}\right) \tag{11}$$

The first term within the parentheses represents the contribution of the change in flux j to the change in caliber A, with a weight of

$$w_1 = \frac{1}{j}\frac{dj}{dt} = \frac{1}{j_{in}}\frac{dj_{in}}{dt} = \frac{2.15\, e^{-0.207\, t}}{21.7 - 10.4\, e^{-0.207\, t}} \tag{12}$$

At equilibrium, i.e. for a constant influx, the retrograde flux and the influx (i.e., the anterograde flux) are related through $j_r = (\gamma_{ar}/\gamma_{ra})\, j_{in}$ and hence $j = j_{in}\left(1 - \frac{\gamma_{ar}}{\gamma_{ra}}\right)$. This relation holds very well during radial growth and allows us to replace j with j_{in} (Eq. 6) in Eq. 12.

The second term within the parentheses in Eq. 11 represents the contribution of the change in average velocity $\bar{v}$ to the change in caliber A, with a weight of

$$w_2 = -\frac{1}{\bar{v}}\frac{d\bar{v}}{dt} = \frac{0.143\, e^{-0.068\, t}}{0.368 + 2.10\, e^{-0.068\, t}} \tag{13}$$

where we inserted Eq. 7 for the average velocities. Finally, for the relative weighting of the contribution of the flux to the caliber growth, we find

$$w_j \equiv \frac{w_1}{w_1 + w_2} \tag{14}$$

and for the relative weighting of the contribution of the slowing to caliber growth we find

$$w_v \equiv \frac{w_2}{w_1 + w_2} \tag{15}$$

Figure 7 shows the results of this analysis for simulations of axonal growth. The linear increase in the cross-sectional area contrasts with the nonlinear increase in the influx and the nonlinear decrease in the velocity. The influx increases steeply in the early weeks of postnatal development. However, as the axon grows, the rate of increase in the influx slows down while the transport velocity continues to decline. As a result of these changes, increases in the influx are the major driver of axonal radial growth during early postnatal development, with slowing of the neurofilament transport velocity becoming the major driver later in development (Figure 7D).

While Figure 7 shows the contributions of neurofilament influx and slowing to the increment of the axonal caliber during radial growth at any instant in time, it does not tell us the cumulative contribution of influx and slowing to the postnatal growth of the

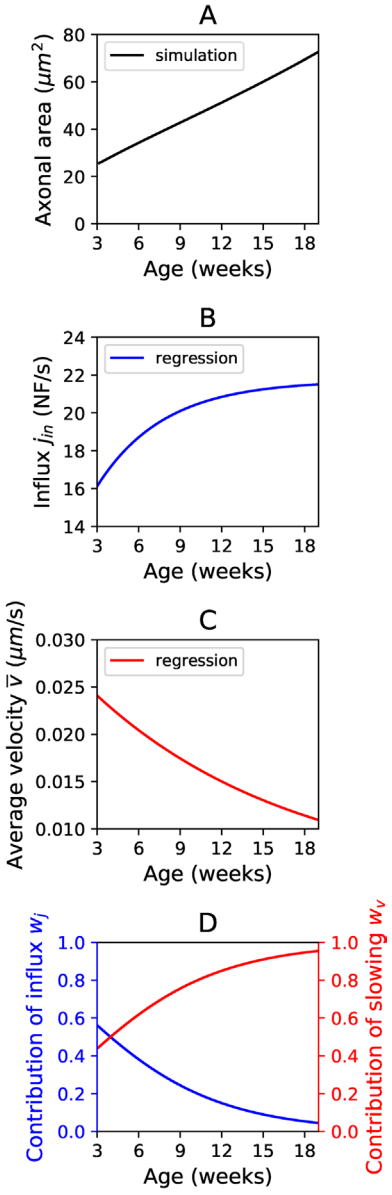

FIGURE 7: The contribution of changes in influx and velocity to the growth of axonal caliber in rat lumbar motor neurons. (A) Growth curve showing the axonal expansion plotted vs. age in weeks. This is the output of our model, which matches the linear regression shown in Eq. 1. (B) Exponential regression for the change in the influx j_{in} vs. age in weeks. (C) Exponential regression for the change in the average velocity $\bar{v}$ (mm/day) vs. age in weeks. (D) The relative contributions of the influx w_j (blue) and the slowing w_v (red) to the growth of axonal caliber between 3 and 18 wk of age.

axon up to that point. To address this, we use the linear regression in Eq. 2 for axons of cross-sectional area >5 μm², extrapolated back to the origin for axons <5 μm² using the polynomial expression in Eq. 3. On the basis of these expressions, we can rewrite Eq. 11 as

$$(dA)_{>5\,\mu m^2} = \frac{1}{\alpha_{NF}} dN_{NF} = \frac{\bar{I}}{\alpha_{NF}}\left(\frac{1}{\bar{v}}dj - \frac{j}{\bar{v}^2}d\bar{v}\right)$$
$$= \frac{\bar{I}}{\alpha_{NF}}\left(1-\frac{\gamma_{ar}}{\gamma_{ra}}\right)\left(\frac{1}{\bar{v}}dj_{in} - \frac{j_{in}}{\bar{v}^2}d\bar{v}\right) \equiv (dA_j + dA_v)_{>5\,\mu m^2} \quad (16)$$

for axons of cross-sectional area >5 μm², and as

$$(dA)_{<5\,\mu m^2} = \frac{dN_{NF}}{79.8 + (3.52)2A} = \frac{\bar{I}}{79.8 + (7.04)A}\left(1-\frac{\gamma_{ar}}{\gamma_{ra}}\right)\left(\frac{1}{\bar{v}}dj_{in} - \frac{j_{in}}{\bar{v}^2}d\bar{v}\right)$$
$$\equiv (dA_j + dA_v)_{<5\,\mu m^2} \quad (17)$$

for axons of cross-sectional area <5 μm², where dA_j is the increment of the axon caliber caused by an increase in influx dj_{in}, and dA_v is the increment caused by a decrease in velocity $d\bar{v}$. Adding all the increments over time results in the cumulative contributions of the influx increase and neurofilament slowing to the growth of axon caliber (A_j and A_v, respectively) in animals ranging from 3 to 18 wk of age. To implement this, we start with an axon of zero cross-sectional area and zero neurofilaments and microtubules and then simulate axon growth using the linear model described above and integrate the incremental contributions of flux and velocity dA_j and dA_v using Eqs. 16 and 17.

The results of this analysis are shown in Figure 8. For 3-wk-old animals, which have an average axonal cross-sectional area of 25 μm², 80% of the postnatal growth in cross-sectional area could be attributed to the increase in neurofilament influx and only 20% to the slowing of neurofilament transport. For 18-wk-old animals, which have an average axonal cross-sectional area of about 69 μm², 60% of the postnatal growth in cross-sectional area could be attributed to slowing. Thus, the increasing rate of influx is the major driver of axonal expansion early in postnatal development, but as the rate of influx stabilizes, the slowing of neurofilament transport becomes more influential.

Radial growth beyond 18 wk

In the experimental data of Hoffman and colleagues on which our modeling study is based, there is a linear increase in the average axonal cross-sectional area from 3 to 18 wk of age. No morphometric data are provided for rats older than 18 wk, but it is reasonable to assume that the radial growth will slow and then plateau as the animals mature further. To estimate the contribution of flux and

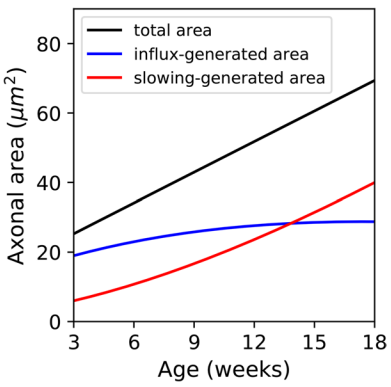

FIGURE 8: Cumulative contribution of flux and slowing to the postnatal growth of axonal caliber. The black line represents the increase in axonal cross-sectional area with age, constrained to match the linear regression in Eq. 1 as described above. The blue line indicates the proportion of the axonal cross-sectional area that can be accounted for by an increase in the neurofilament influx alone. The red line indicates the proportion of the axonal cross-sectional area that can be accounted for by a decrease in the neurofilament transport velocity alone. The increase in axonal caliber can be attributed largely to an increase in neurofilament influx at early times, with a slowing of neurofilament transport becoming more influential at later times.

velocity during this maturation phase, we constrained the average axonal cross-sectional area in our model to approach a constant value of 80 μm^2, (average diameter = 10 μm), which corresponds approximately to the maximum axon diameter extracted from the histograms of axon diameters at 18 wk of age in Figure 5 of Hoffman *et al*. (1985a). The cross-sectional area was assumed to approach this constant value by the exponential regression

$$A = 80.0\ \mu m^2 - 72.5\ \mu m^2 \exp(-0.080\ t) \qquad (18)$$

where time t is measured in weeks (see Figure 9). The neurofilament and microtubule densities were obtained using the same regressions as those used above (Figure 1, B and C).

Using the periodic version of the model, we found that the influx and neurofilament transport velocities approach finite constant values as the axons approach their target caliber (Figure 9, B and C). Thus, neurons can tune their axon caliber during postnatal development by coordinated regulation of the flux and velocity of neurofilament transport.

DISCUSSION

Neurofilaments are space-filling structures that are separated from each other by radial sidearm projections that maximize the axonal volume occupied by each polymer. As neurofilaments accumulate in axons, they contribute to the expansion of axon caliber in proportion to their number. Most of this accumulation occurs after birth, coincident with the onset of myelination. In large myelinated axons, which can contain several thousand neurofilaments per cross-section, these polymers occupy most of the axonal volume and thus make a significant contribution to the axonal caliber. Because neurofilaments are delivered to axons by the mechanisms of axonal transport, it has been hypothesized that the neurofilament content of the axon is determined by the volume and kinetics of neurofilament transport and thus that there is a direct relationship between neurofilament transport and axon caliber (Hoffman, 1995). To test the feasibility of this hypothesis, we developed a computational model of neurofilament transport that relates the influx and transport kinetics of axonal neurofilaments to the axonal cross-sectional area.

The kinetic states of our model were based on our prior kinetic and computational analyses of neurofilament transport in cultured nerve cells, in which we have shown that axonal neurofilaments alternate between distinct short-term and long-term pausing states that we term on- and off-track, respectively. Neurofilaments in the on-track state exhibit short bouts of rapid movement interrupted by short pauses, whereas neurofilaments in the off-track state pause for prolonged periods without movement. Because neurofilaments greatly outnumber microtubules in large neurofilament-rich axons, most neurofilaments are not adjacent to a microtubule. For these neurofilaments to move, they must make a diffusional encounter with a microtubule track. Thus, in our model we assume that neurofilaments are mobile in the radial dimension of the axon and that the rate of engagement of off-track neurofilaments with their microtubule tracks is governed by the rate of diffusion of the neurofilaments in the cross-sectional plane of the axon and the average distance between the neurofilaments and the microtubules. We use this model to simulate the radial growth of myelinated motor axons of rat lumbar ventral root and sciatic nerve during postnatal development, constraining the model to match published morphometric data on axon caliber and neurofilament and microtubule densities in L5 ventral roots of these animals as well as radioisotopic pulse-labeling studies of neurofilament transport in the lumbar ventral root and sciatic nerve. Assuming that the axon caliber and microtubule densities are uniform along the axons, we show that the model can explain the published data of Hoffman and colleagues on the growth of axon caliber and kinetics of neurofilament transport during the postnatal development of rat lumbar motor neurons.

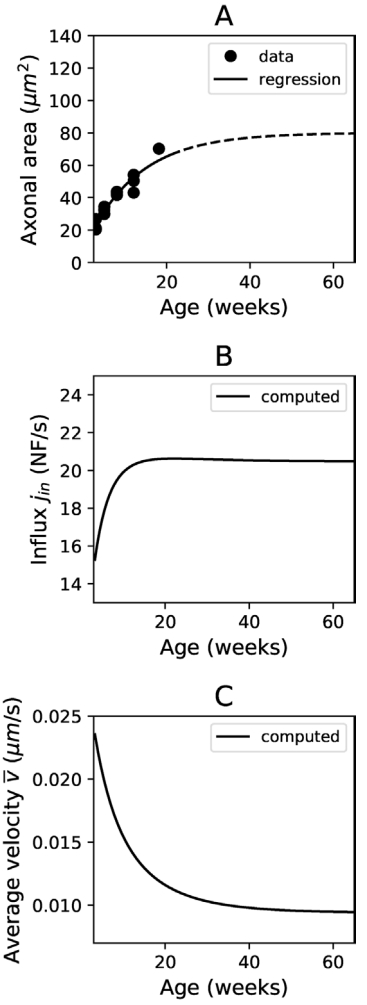

FIGURE 9: Simulation of the neurofilament transport changes that accompany axonal maturation. (A) Extrapolation of the radial axonal growth to an asymptotic cross-sectional area of 80.0 μm^2 using the exponential regression in Eq. 18. The line represents the regression and is dashed beyond 21 wk to denote that it is an extrapolation for these ages. (B) The time course of the influx predicted by the model. (C) The time course of the average neurofilament transport rate predicted by the model. The data points in A represent the experimental data, and the line represents the regression in Eq. 18.

Because postnatal axonal development is accompanied by an increase in neurofilament gene expression and a slowing of neurofilament transport, it has long been assumed that the radial growth of axons can be explained by changes in neurofilament influx and transport velocity (Hoffman, 1995). Our study confirms this quantitatively and also provides the first quantitative estimate of their relative contributions. We found that the answer is time dependent and evolves during postnatal development. Initially, the radial growth can be attributed primarily to the rapid increase in neurofilament influx, while later in development the influx plateaus and slowing of neurofilament transport becomes the dominant contributor. This transition from an expression-driven phase of radial growth to a slowing-driven phase results in continued expansion of axon caliber even after the rate of neurofilament influx stabilizes.

An additional outcome of our study is a prediction of the magnitude of the neurofilament influx into the axon, which is a parameter that has never been measured experimentally. Our simulations predict an influx of approximately 21 neurofilaments per second for the average myelinated axon at 18 wk of age, assuming a neurofilament length of 5 μm. Because the average neurofilament content of these axons at this age was approximately 8000 per cross-section, this represents about 0.26% of the total neurofilament content. This low rate of flux reflects the slow average velocity of neurofilament transport and is approximately consistent with our previous modeling studies in adult mouse sciatic nerve, which have indicated that at any point in time only 0.5% of the filaments are moving in myelinated internodes (Walker *et al.*, 2019).

It is important to note that neurofilament number may not be the sole determinant of axonal caliber in large myelinated axons. For example, neurofilament density is not uniform across all axons and appears to be influenced by the polypeptide composition of filaments and the phosphorylation of their carboxy-terminal neurofilament side arm projections (Nixon *et al.*, 1994; Garcia *et al.*, 2003; Mukhopadhyay *et al.*, 2004; Chang *et al.*, 2009; Malka-Gibor *et al.*, 2017). In addition, recent evidence indicates that axon caliber is also influenced by the membrane-associated periodic cytoskeleton, which consists of regularly spaced actin filament rings associated with the cytosolic surface of the plasma membrane and linked by spectrin molecules (He *et al.*, 2016). These rings provide structural support to the axonal plasma membrane and also influence axon diameter and physiology, microtubule dynamics, and vesicle transport (Costa *et al.*, 2018; Costa and Sousa, 2021). Many questions remain, however, about the extent of cross-talk between this membrane cytoskeleton and other cytoskeletal components. For example, mice lacking a component of the membrane-associated periodic cytoskeleton called adducin have increased caliber and actin ring diameter but also a higher neurofilament density, implying an increased neurofilament content (Leite *et al.*, 2016). This suggests that alterations to the membrane-associated periodic cytoskeleton may influence neurofilament transport and/or gene expression. On the other hand, axonal expansion in response to changes in neurofilament content must be accompanied by expansion of the actin rings, indicating that the membrane cytoskeleton is also capable of dynamic remodeling in response to changes in neurofilament content. Thus, the membrane-associated periodic cytoskeleton may both influence and respond to changes in axon caliber.

A key feature of our computational model is that it is able to explain the slowing of neurofilament transport during rat postnatal development in terms of the decline in microtubule density. Importantly, this slowing is not an assumption in our model but rather emerges as the axons expand because the increase in the number of microtubules does not keep pace with the increase in the number of neurofilaments and thus, over time, the accessibility of neurofilaments to their microtubule tracks declines. This, in turn, results in a decrease in the on-rate. Because the increase in neurofilament content arises due to the increase in neurofilament influx, the slowing of neurofilament transport during postnatal development can be considered a simple consequence of the increase in the neurofilament influx. If the microtubule number were to increase in direct proportion to the neurofilament number during postnatal development, then the microtubule density would remain unchanged. There would be no decline in neurofilament transport, and the radial growth of the axons would be entirely dependent on the neurofilament influx. While this proposed mechanism of neurofilament slowing remains to be proven experimentally, it is consistent with experimental observations on the correlation between the kinetics of neurofilament transport and the neurofilament:microtubule ratio during axon regeneration after injury. Specifically, axonal injury results in a decline in neurofilament gene expression, a decrease in axon caliber, and an increase in both microtubule density and neurofilament transport velocity (Hoffman *et al.*, 1984). It is also supported by our studies of neurofilament transport across nodes of Ranvier, where there is a local constriction of the axon accompanied by a decrease in neurofilament number and an increase in both microtubule density and neurofilament transport velocity (Walker *et al.*, 2019; Ciocanel *et al.*, 2020). Thus, microtubule density may be a basic regulator of neurofilament transport.

It is interesting to consider why neurofilament transport slows during postnatal development, or indeed, why slow axonal transport is so slow at all. The answer appears to be that the purpose of slow axonal transport is to distribute proteins along the axon rather than to deliver them to the axon tip (Brown, 2003). With this purpose in mind, speed is not necessarily an advantage and actually comes with a significant energetic cost in terms of both the production and the movement of the cargoes. Thus, the slow transport of neurofilaments in axons could be considered a more efficient solution to the problem of delivering and distributing these polymers. By the same reasoning, the slowing of neurofilament transport during postnatal development may be an adaptation to permit the axon to reach its target caliber while producing and moving fewer neurofilaments, thereby lowering the metabolic cost of establishing the desired axon caliber.

A central assumption in our model is that all the neurofilaments in axons move and thus changes in neurofilament transport result directly in changes in neurofilament content. As discussed above, the results of our simulations support this assumption. However, some researchers have proposed that the majority of axonal neurofilaments are deposited into a permanently stationary cytoskeleton and that radioisotopic pulse-labeling experiments reflect the movement of only a small proportion of the total axonal neurofilament population (Nixon and Logvinenko, 1986; Yuan *et al.*, 2009, 2017). If only a small proportion of axonal neurofilaments are mobile, then the kinetics of neurofilament transport might not correlate directly with the neurofilament content. In support of their hypothesis, these researchers reported several examples of mutant mice in which the neurofilament content of optic nerve axons differed from that in wild-type mice but the kinetics of neurofilament transport did not (Yuan *et al.*, 2015). The three lines of mice examined were a transgenic line overexpressing human NFH, a transgenic line overexpressing a mutant human NFL, and an NFH knockout line. Interpretation of the data from these mice is complicated by the fact that the mechanism by which these mutations lead to differences in neurofilament content is not clear. However, setting aside that concern, it is not possible to relate the abundance of neurofilaments ρ to their transport velocity $\bar{v}$ without knowing the flux j because $j = \rho\bar{v}$. For example, if an axon has twice the neurofilament content, the neurofilament velocity can still be the same if it also has twice the flux. Hence differences in the neurofilament content of axons in different lines of mice could be explained by difference in the neurofilament flux with no difference in the neurofilament transport velocity. Thus, we would caution against simply equating neurofilament content and transport kinetics without taking into consideration neurofilament flux.

METHODS

In this section we describe the source of the experimental data that we use, how we model the transport kinetics of neurofilaments, how we account for the axonal cross-sectional area based on the abundance of the constituent neurofilaments and microtubules, how we

extract the flux, and how we simulate the movement of radiolabeled neurofilaments to compare our model with radioisotopic pulse-labeling experiments on a timescale of days and weeks.

Experimental data

We used experimental data published in a series of papers by Hoffman, Price, and colleagues on the postnatal development of myelinated motor axons in the L5 ventral root and sciatic nerve of rats (Hoffman *et al.*, 1983, 1984, 1985a,b). Collectively, these papers provide a unique opportunity for our modeling study because they report morphometric measurements on neurofilament and microtubule densities and the growth of axon caliber, as well as kinetic data on neurofilament transport obtained using radioisotopic pulse labeling, all at multiple time points spanning the first 5 mo of life in these animals. For the radioisotopic pulse-labeling kinetics, we used data obtained by isotope injection into rats at 3 and 12 wk of age from Figures 2 and 3 in Hoffman *et al.* (1985a). For the myelinated axon caliber, we used the data obtained in L5 ventral roots of rats at 3, 5, 8, 12, and 18 wk of age from Figure 6 in Hoffman *et al.* (1985a). For the neurofilament and microtubule densities, we used the data obtained in L5 ventral roots of rats at 3, 5, 8, 12, and 18 wk of age from Figure 10 in Hoffman *et al.* (1984). The data were extracted from the published figures using WebPlotDigitizer (Ankit Rohatgi, version 4.5, August 2021).

Mathematical model of the neurofilament transport kinetics

We simulated neurofilament transport using the six-state model described previously (Jung and Brown, 2009). This model emerged from two sets of experiments, one where the motion of single neurofilaments was tracked along axons on a timescale of minutes using time-lapse fluorescence imaging (Wang *et al.*, 2000; Brown *et al.*, 2005) and another one where a pulse of fluorescently activated neurofilaments was tracked on a timescale of several hours using a fluorescence photoactivation strategy (Trivedi *et al.*, 2007). These studies revealed that neurofilaments switch between distinct pausing states that we termed on-track and off-track. Neurofilaments in the on-track state are engaged with their microtubule tracks and move in rapid bursts interspersed by brief pauses on the order of seconds to minutes in length. In contrast, neurofilaments in the off-track state pause for long periods of time on the order of hours, functionally disengaged and perhaps also physically distant from their microtubule tracks.

We have shown that this motile behavior can be described using a kinetic model in which each filament moves independently and bidirectionally along the length of the axon, cycling between six states. In the on-track moving states *a* and *r*, the neurofilaments move anterogradely and retrogradely along microtubule tracks with constant velocities v_a and v_r, respectively. In the on-track pausing states a_0 and r_0, the filaments pause for brief periods of time that last for seconds to minutes. On-track filaments switch repeatedly between these moving and short-term pausing states governed by rates γ_{10} and γ_{01}, resulting in "stop-and-go" intermittent motion of neurofilaments along their microtubule tracks (Brown *et al.*, 2005). While pausing on-track, the neurofilaments can also disengage from their microtubule tracks and enter the long-term anterograde or retrograde pausing states, a_p or r_p, at a rate determined by the rate constant γ_{off}. They can reengage with a microtubule at a rate determined by the rate constant γ_{on}. While pausing on- or off-track, the neurofilaments can change direction governed by the anterograde-to-retrograde and retrograde-to-anterograde "reversal rates" γ_{ar} and γ_{ra}, respectively. This scheme is summarized graphically in Figure 10. The following set of partial differential equations describes the distribution of neurofilaments in the six kinetic states

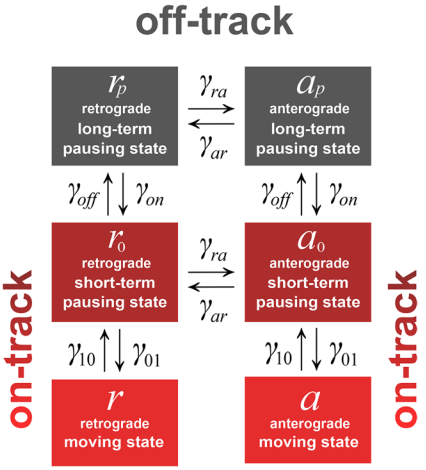

FIGURE 10: The six-state model of axonal neurofilament transport. An "on-track" neurofilament can transition from anterograde or retrograde moving states (*a* or *r*) to corresponding short-term pausing states (a_0 or r_0) while still bound to a microtubule track (governed by the rate constants γ_{10} and γ_{01}). During a short-term pause, the neurofilament can detach from the microtubule track and enter the corresponding "off-track" long-term pausing states (a_p or r_p). Note that we define separate anterograde and retrograde off-track pausing states so that we can separate reversals (governed by the rate constants γ_{ar} and γ_{ra}) from switching between on- and off-track states (governed by the rate constants γ_{on} and γ_{off}). The neurofilaments can reverse direction in either the on-track or the off-track pausing states. Adapted from Jung and Brown (2009).

with respect to distance *x* along the axon and time *t*, governed by the six rate constants, for the anterograde direction:

$$\begin{aligned}
\frac{\partial \rho_a}{\partial t} &= -v_a \frac{\partial \rho_a}{\partial x} - \gamma_{10}\rho_a(x,t) + \gamma_{01}\rho_{a0}(x,t)\\
\frac{\partial \rho_{a0}}{\partial t} &= -(\gamma_{01} + \gamma_{ar} + \gamma_{off})\,\rho_{a0}(x,t) + \gamma_{10}\rho_a(x,t) + \gamma_{ra}\rho_{r0}(x,t) + \gamma_{on}\rho_{ap}(x,t)\\
\frac{\partial \rho_{ap}}{\partial t} &= \gamma_{off}\rho_{a0}(x,t) - (\gamma_{on} + \gamma_{ar})\,\rho_{ap}(x,t) + \gamma_{ra}\rho_{rp}(x,t)
\end{aligned} \tag{19}$$

where ρ_a, ρ_{a0}, and ρ_{ap} are the linear densities of neurofilaments in the anterograde moving and short-term and long-term pausing states respectively, and for the retrograde direction:

$$\begin{aligned}
\frac{\partial \rho_r}{\partial t} &= -v_r \frac{\partial \rho_r}{\partial x} - \gamma_{10}\rho_r(x,t) + \gamma_{01}\rho_{r0}(x,t)\\
\frac{\partial \rho_{r0}}{\partial t} &= -(\gamma_{01} + \gamma_{ra} + \gamma_{off})\,\rho_{r0}(x,t) + \gamma_{10}\rho_r(x,t) + \gamma_{ar}\rho_{a0}(x,t) + \gamma_{on}\rho_{rp}(x,t)\\
\frac{\partial \rho_{rp}}{\partial t} &= \gamma_{off}\rho_{r0}(x,t) - (\gamma_{on} + \gamma_{ra})\,\rho_{rp}(x,t) + \gamma_{ar}\rho_{ap}(x,t)
\end{aligned} \tag{20}$$

where ρ_r, ρ_{r0}, and ρ_{rp} are the corresponding linear densities of neurofilaments in the retrograde moving and short-term and long-term pausing states, respectively.

Computational implementation of the model

To simulate neurofilament transport and the growth of axonal caliber during postnatal development, the mathematical six-state model was converted to a computational one using a spatial and temporal discretization. The distance along an axon of length *L* was divided into a total of *N* bins, each of length Δx. Time *t* was

discretized into short time intervals of Δt. For the simulations presented in this study, we used $\Delta x = 1$ µm and $\Delta t = 1$ s. The distance at any point along the axon is then the position of the ith bin relative to the zeroth bin at the proximal end of the axon ($x_0 = 0$), i.e.

$$x_i = x_0 + i\Delta x \tag{21}$$

We apply a forward-time and backward-space discretization scheme to the three partial differential equations describing the distributions of neurofilaments in the anterograde direction in Eq. 19, resulting in the following set of equations that describe the time evolution of the anterograde linear distributions of the neurofilaments along the axon across all kinetic states:

$$\begin{aligned}
\rho_a(x_i, t+\Delta t) &= \rho_a(x_i, t) - v_a \frac{\Delta t}{\Delta x}\left(\rho_a(x_i, t) - \rho_a(x_{i-1}, t)\right) \\
&\quad + \Delta t\left(\gamma_{01}\,\rho_{a0}(x_i, t) - \gamma_{10}\,\rho_a(x_i, t)\right) \\
\rho_{a0}(x_i, t+\Delta t) &= \rho_{a0}(x_i, t) + \Delta t\left(\gamma_{10}\,\rho_a(x_i, t) + \gamma_{ra}\,\rho_{r0}(x_i, t)\right. \\
&\quad \left. + \gamma_{on}\,\rho_{ap}(x_i, t) - \left(\gamma_{01} + \gamma_{ar} + \gamma_{off}\right)\rho_{a0}(x_i, t)\right) \\
\rho_{ap}(x_i, t+\Delta t) &= \rho_{ap}(x_i, t) + \Delta t\left(-\left(\gamma_{on} + \gamma_{ar}\right)\rho_{ap}(x_i, t)\right. \\
&\quad \left. + \gamma_{off}\,\rho_{a0}(x_i, t) + \gamma_{ra}\,\rho_{rp}(x_i, t)\right)
\end{aligned} \tag{22}$$

Similarly, we apply a forward-time and backward-space discretization for the equations in the retrograde direction in Eq. 20, resulting in the following set of equations for the retrograde linear distributions of the neurofilaments along the axon across all states:

$$\begin{aligned}
\rho_r(x_i, t+\Delta t) &= \rho_r(x_i, t) - v_r \frac{\Delta t}{\Delta x}\left(\rho_r(x_{i+1}, t) - \rho_r(x_i, t)\right) \\
&\quad + \Delta t\left(\gamma_{01}\,\rho_{r0}(x_i, t) - \gamma_{10}\,\rho_r(x_i, t)\right) \\
\rho_{r0}(x_i, t+\Delta t) &= \rho_{r0}(x_i, t) + \Delta t\left(\gamma_{10}\,\rho_r(x_i, t) + \gamma_{ar}\,\rho_{a0}(x_i, t)\right. \\
&\quad \left. + \gamma_{on}\,\rho_{rp}(x_i, t) - \left(\gamma_{01} + \gamma_{ra} + \gamma_{off}\right)\rho_{r0}(x_i, t)\right) \\
\rho_{rp}(x_i, t+\Delta t) &= \rho_{rp}(x_i, t) + \Delta t\left(-\left(\gamma_{on} + \gamma_{ra}\right)\rho_{rp}(x_i, t)\right. \\
&\quad \left. + \gamma_{off}\,\rho_{r0}(x_i, t) + \gamma_{ar}\,\rho_{ap}(x_i, t)\right)
\end{aligned} \tag{23}$$

We impose the boundary conditions $\rho_\eta(x_N, t) = \rho_\eta(x_{N-1}, t)$ at the distal end of the axon, simulating an infinitely long axon using a finite model where all linear distributions of neurofilaments, i.e. $\rho_\eta(x)$ with $\eta = a, a_0, a_p, r, r_0, r_p$, are uniform and in steady state. We consider the center point of a filament of length l_{NF}, such that it extends across $l_{NF}/(2\Delta x)$ bins on each side. We find the number of neurofilaments in any given bin in the axon by adding up the linear distributions of neurofilaments that are occupying that bin plus the $l_{NF}/(2\Delta x)$ bins on each side, i.e. $(l_{NF} + \Delta x)/\Delta x$ bins in total, across all kinetic states. The number of neurofilaments N_{NF} at any given location in a homogeneous axon is therefore given by

$$N_{NF}(x_i) = \frac{\overline{l}}{\Delta x}\rho_{total}(x_i) \tag{24}$$

where $\Delta x = 1$ µm, $\rho_{total} = \rho_a + \rho_{a0} + \rho_{ap} + \rho_r + \rho_{r0} + \rho_{rp}$ and $\overline{l} = l_{NF} + \Delta x$. The average length of neurofilaments in vivo is not known so we assume that all neurofilaments have the same length of $l_{NF} = 5$ µm, which is the approximate average length of moving neurofilaments in cultured nerve cells (Fenn *et al.*, 2018).

The resulting model mimics the neurofilament transport kinetics observed experimentally (Brown *et al.*, 2005; Jung and Brown, 2009). To apply this model to the radial growth of an axon, we considered the axon to be a cylinder with a cross-sectional area A containing N_{MT} microtubules and N_{NF} neurofilaments. During postnatal maturation, the cylinder accommodates an increasing number of neurofilaments, leading to its radial expansion, i.e. an increase in caliber A. In the present study, we considered that one of the mechanisms for this accumulation was an increase in the influx j_{in} of neurofilaments from the cell body associated with an increase in neurofilament gene expression. The influx is defined as the average number of neurofilaments that enter the axon in a unit of time. We simulated this influx at the proximal end ($x_0 = 0$) by increasing the density of anterogradely moving neurofilaments $\rho_a(x_0, t+\Delta t)$ in the zeroth bin as follows:

$$\begin{aligned}
\rho_a(x_0, t+\Delta t) &= \rho_a(x_0, t) + \Delta t\left(-\frac{v_a}{\Delta x}\rho_a(x_0, t) + \frac{j_{in}}{\Delta x}\right. \\
&\quad \left. + \gamma_{01}\rho_{a0}(x_0, t) - \gamma_{10}\rho_a(x_0, t)\right)
\end{aligned} \tag{25}$$

To obtain the average velocity of all neurofilaments in any bin i, we summed the fractions of the neurofilament population in the anterograde and retrograde moving states multiplied by their respective velocities, i.e.

$$v(x_i) = \frac{\rho_a(x_i)v_a + \rho_r(x_i)v_r}{\rho_{total}(x_i)} \tag{26}$$

The neurofilaments move bidirectionally, resulting in an anterograde flux j_a, a retrograde flux j_r, and a net-flux $j = j_a + j_r$. These fluxes, which have the dimensions 1/s and describe the number of neurofilaments that pass an axonal cross-section at position x_i in a unit of time, were extracted from the computational model as follows:

$$\begin{aligned}
j_a(x_i) &= \rho_a(x_i)v_a \\
j_r(x_i) &= \rho_r(x_i)v_r
\end{aligned} \tag{27}$$

The microtubule density determines the on-rate

As described above, we consider neurofilaments in the off-track states to be disengaged from their microtubule tracks and hence not capable of transport along the axon. For these neurofilaments to move, they must first find a microtubule. In our model, this is governed by the rate constant γ_{on}. Because neurofilaments outnumber microtubules in myelinated axons (Price *et al.*, 1988; Reles and Friede, 1991), this likely requires movement in the radial dimension of the axon. We modeled this as diffusion in the cross-sectional plane of the axon.

In a recent study, Chakrabarty (2020) assumed off-track neurofilaments to be capable of lateral diffusion, as if engaged in a constant radial diffusive search for an available microtubule track. Chakrabarty (2020) calculated the resulting binding rate, which is equivalent to the on-rate γ_{on} in our model. The results showed that the rate exhibited a 3/2 power-law dependence on the density of the available microtubules ρ_{MT}, i.e.

$$\gamma_{on} = 2\overline{d}\sqrt{\pi}D_{NF}\sum_{i=1}^{\infty}\left(\frac{(i-1)!}{\Gamma\left(i+\frac{1}{2}\right)}\right)^3\rho_{MT}^{3/2} \tag{28}$$

where $\overline{d} = 2r_{NF} + 2r_{MT}$ is the sum of the diameters of a neurofilament and a microtubule and is twice the distance between these polymers when a neurofilament is on-track, and D_{NF} is the diffusion coefficient of neurofilaments in the radial dimension of the axon. The microtubule density ρ_{MT} is defined as the number of microtubules

divided by the axonal cross-sectional area and is assumed to be random, with an equal probability of finding a microtubule at all locations across the axon cross-section. The above expression neglects interactions between neurofilaments, which would be expected to result in a smaller effective diffusion constant (van Beijeren and Kutner, 1985; Novak *et al.*, 2009). However, because we calibrate the unknown diffusion coefficient to the actual initial neurofilament velocity observed experimentally (see *Results*), such crowding effects are incorporated implicitly into our model.

Note that an increase in the microtubule density will decrease the average distance between neurofilaments and their nearest microtubule track, and thus off-track neurofilaments will move on-track more quickly, resulting in a larger on-rate γ_{on} and a faster average transport velocity. To implement the varying on-rate computationally during our simulations of radial axonal growth, we assume each microtubule track has the capacity to accommodate up to $p = 5$ neurofilaments, and we take the neurofilament and microtubule radii to be $r_{NF} = 20.0$ nm and $r_{MT} = 12.5$ nm (Xue *et al.*, 2015). Denoting the number of neurofilaments engaged with microtubules at a location x along the axon by N_{on} and the total number of microtubules not available to bind additional neurofilaments by N_{on}/p, the on-rate assumes the form

$$\gamma_{on} = 4.63\sqrt{\pi}D_{NF}\left(\frac{N_{MT} - N_{on}/p}{Area}\right)^{3/2} \tag{29}$$

where $N_{on} = (\rho_a + \rho_{a0} + \rho_r + \rho_{r0})\,\overline{l}$ is the number of all neurofilaments in the on-track states.

Finding the influx

To examine the possible role of temporal changes in neurofilament export from the cell body for the growth of axon caliber, we use Eq. 25 to simulate an injection of neurofilaments with influx j_{in} into the proximal end of the axon. No direct experimental data for the neurofilament influx in vivo are available, but we are able to infer it computationally based on the axonal neurofilament and microtubule content. One way to do this would be to systematically change the influx in the model until the desired neurofilament and cross-sectional area are identified. A more efficient method is to create a periodic version of the model in which the neurofilaments that leave the axon distally enter it again proximally and vice versa, effectively creating a closed loop (Figure 2B). To implement this model, we consider a short (1 mm) length of axon of the desired caliber and distribute neurofilaments and microtubules uniformly along this axon so that their density is consistent with the morphometric data (see below). We then simulate neurofilament transport using the six-state model described above and allow the system to equilibrate. As the neurofilaments traverse the axon in a periodic manner, the average velocity $\overline{v}$, anterograde flux $j_a = \rho_a v_a$, retrograde flux $j_r = \rho_r v_r$, and net flux $j = j_a + j_r$ emerge directly from the simulations.

To connect back to the linear version of the model (Figure 2A) in which there is a net addition of neurofilaments proximally and a net loss distally, we have to specify only the influx j_{in} determined from the periodic model above, i.e.

$$j_{in} = j_a = \rho_a v_a \tag{30}$$

and then the retrograde and net fluxes j_r and $j = j_a + j_r$ emerge from the resulting simulations.

Simulating the propagation of radiolabeled neurofilaments

To simulate the movement of a pulse of radiolabeled neurofilaments computationally in a radioisotopic pulse-labeling experiment, we model a single axon that can be thought of as an average of the many axons that make up a nerve in the animal. We split the total influx j_{in} into two populations, one that is labeled and another that is nonlabeled:

$$j_{in} = j_{lab} + j_{non} \tag{31}$$

where j_{lab} is the influx of labeled neurofilaments and j_{non} is the influx of nonlabeled neurofilaments. We now have two sets of six-state equations, one for the labeled neurofilaments and the other for the nonlabeled neurofilaments, i.e.

$$\begin{aligned}
\rho_{a,lab}(x_0, t+\Delta t) &= \rho_{a,lab}(x_0,t) + \Delta t\Big(-\frac{v_a}{\Delta x}\rho_{a,lab}(x_0,t) + \frac{j_{lab}}{\Delta x} \\
&\quad + \gamma_{01}\rho_{a0,lab}(x_0,t) - \gamma_{10}\rho_{a,lab}(x_0,t)\Big) \\
\rho_{a,lab}(x_i, t+\Delta t) &= \rho_{a,lab}(x_i,t) + \Delta t\Big(-\frac{v_a}{\Delta x}\big(\rho_{a,lab}(x_i,t) - \rho_{a,lab}(x_{i-1},t)\big) \\
&\quad + \gamma_{01}\rho_{a0,lab}(x_i,t) - \gamma_{10}\rho_{a,lab}(x_i,t)\Big) \\
\rho_{a0,lab}(x_i, t+\Delta t) &= \rho_{a0,lab}(x_i,t) + \Delta t\big(\gamma_{10}\rho_{a,lab}(x_i,t) + \gamma_{ra}\rho_{r0,lab}(x_i,t) \\
&\quad + \gamma_{on}\rho_{ap,lab}(x_i,t) - (\gamma_{01} + \gamma_{ar} + \gamma_{off})\,\rho_{a0,lab}(x_i,t)\big) \\
\rho_{ap,lab}(x_i, t+\Delta t) &= \rho_{ap,lab}(x_i,t) + \Delta t\big(\gamma_{off}\rho_{a0,lab}(x_i,t) \\
&\quad - (\gamma_{on} + \gamma_{ar})\rho_{ap,lab} + \gamma_{ra}\rho_{rp,lab}(x_i,t)\big) \\
\rho_{r,lab}(x_i, t+\Delta t) &= \rho_{r,lab}(x_i,t) + \Delta t\Big(-\frac{v_r}{\Delta x}\big(\rho_{r,lab}(x_{i+1},t) - \rho_{r,lab}(x_i,t)\big) \\
&\quad + \gamma_{01}\rho_{r0,lab}(x_i,t) - \gamma_{10}\rho_{r,lab}(x_i,t)\Big) \\
\rho_{r0,lab}(x_i, t+\Delta t) &= \rho_{r0,lab}(x_i,t) + \Delta t\big(\gamma_{10}\rho_{r,lab}(x_i,t) + \gamma_{ar}\rho_{a0,lab}(x_i,t) \\
&\quad + \gamma_{on}\rho_{rp,lab}(x_i,t) - (\gamma_{01} + \gamma_{ra} + \gamma_{off})\,\rho_{r0,lab}(x_i,t)\big) \\
\rho_{rp,lab}(x_i, t+\Delta t) &= \rho_{rp,lab}(x_i,t) + \Delta t\big(-(\gamma_{on} + \gamma_{ra})\rho_{rp,lab}(x_i,t) \\
&\quad + \gamma_{off}\rho_{r0,lab}(x_i,t) + \gamma_{ar}\rho_{ap,lab}(x_i,t)\big)
\end{aligned} \tag{32}$$

and

$$\begin{aligned}
\rho_{a,non}(x_0, t+\Delta t) &= \rho_{a,non}(x_0,t) + \Delta t\Big(-\frac{v_a}{\Delta x}\rho_{a,non}(x_0,t) + \frac{j_{non}}{\Delta x} \\
&\quad + \gamma_{01}\rho_{a0,non}(x_0,t) - \gamma_{10}\rho_{a,non}(x_0,t)\Big) \\
\rho_{a,non}(x_i, t+\Delta t) &= \rho_{a,non}(x_i,t) + \Delta t\Big(-\frac{v_a}{\Delta x}\big(\rho_{a,non}(x_i,t) - \rho_{a,non}(x_{i-1},t)\big) \\
&\quad + \gamma_{01}\rho_{a0,non}(x_i,t) - \gamma_{10}\rho_{a,non}(x_i,t)\Big) \\
\rho_{a0,non}(x_i, t+\Delta t) &= \rho_{a0,non}(x_i,t) + \Delta t\,\big(\gamma_{10}\rho_{a,non}(x_i,t) + \gamma_{ra}\rho_{r0,non}(x_i,t) \\
&\quad + \gamma_{on}\rho_{ap,non}(x_i,t) - (\gamma_{01} + \gamma_{ar} + \gamma_{off})\,\rho_{a0,non}(x_i,t)\big) \\
\rho_{ap,non}(x_i, t+\Delta t) &= \rho_{ap,non}(x_i,t) + \Delta t\,\big(\gamma_{off}\rho_{a0,non}(x_i,t) \\
&\quad - (\gamma_{on} + \gamma_{ar})\rho_{ap,non} + \gamma_{ra}\rho_{rp,non}(x_i,t)\big) \\
\rho_{r,non}(x_i, t+\Delta t) &= \rho_{r,non}(x_i,t) + \Delta t\Big(-\frac{v_r}{\Delta x}\big(\rho_{r,non}(x_{i+1},t) - \rho_{r,non}(x_i,t)\big) \\
&\quad + \gamma_{01}\rho_{r0,non}(x_i,t) - \gamma_{10}\rho_{r,non}(x_i,t)\Big) \\
\rho_{r0,non}(x_i, t+\Delta t) &= \rho_{r0,non}(x_i,t) + \Delta t\,\big(\gamma_{10}\rho_{r,non}(x_i,t) + \gamma_{ar}\rho_{a0,non}(x_i,t) \\
&\quad + \gamma_{on}\rho_{rp,non}(x_i,t) - (\gamma_{01} + \gamma_{ra} + \gamma_{off})\,\rho_{r0,non}(x_i,t)\big) \\
\rho_{rp,non}(x_i, t+\Delta t) &= \rho_{rp,non}(x_i,t) + \Delta t\,\big(-(\gamma_{on} + \gamma_{ra})\rho_{rp,non}(x_i,t) \\
&\quad + \gamma_{off}\rho_{r0,non}(x_i,t) + \gamma_{ar}\rho_{ap,non}(x_i,t)\big)
\end{aligned} \tag{33}$$

As a result, the two neurofilament populations propagate along the axon, each cycling between the six kinetic states according to the same rate constants as defined above. The wave of labeled neurofilaments is the sum of the distributions of the labeled neurofilaments in all six kinetic states, i.e.

$$\rho_{lab} = \rho_{a,lab} + \rho_{a0,lab} + \rho_{ap,lab} + \rho_{r,lab} + \rho_{r0,lab} + \rho_{rp,lab} \quad (34)$$

For the simulations, we used a square wave pulse of labeled filaments and set the duration of the pulse to 6 h based on a previous computational modeling study of neurofilament transport in mouse optic nerve (Li *et al*., 2012). However, we should note that the precise duration and shape of this pulse has little influence on the shape of the resulting wave because it spreads enormously due to the stochastic and bidirectional nature of the neurofilament movement. To ignore events that determine neurofilament fate at the distal ends of the axons, the length of the axon was assumed to be very long, specifically 20 cm.

Code availability

The code will be made available upon reasonable request. Requests should be submitted to the corresponding authors.

ACKNOWLEDGMENTS

We thank Paul Hoffman for helpful discussions on the topic of neurofilament transport and the radial growth of axons. This project would not have been possible without the experimental data provided by his body of published work. R.M.N. was supported in part by a scholarship from the Fulbright Foreign Student Program. This project was funded in part by collaborative National Science Foundation grants IOS1656784 and IOS1656765 to A.B. and P.J. and National Institutes of Health grant R01 NS038526 to A.B.

REFERENCES

Berthold C, Rydmark M (1995). Morphology of normal peripheral axons. In: The Axon-Structure, Function and Pathophysiology, New York, NY: Oxford University Press, 13–48.

Boyer NP, Julien JP, Jung P, Brown A (2022). Neurofilament transport is bidirectional in vivo. eNeuro 9, ENEURO.0138–22.2022.

Brown A (2000). Slow axonal transport: stop and go traffic in the axon. Nat Rev Mol Cell Biol 1, 153–156.

Brown A (2003). Axonal transport of membranous and nonmembranous cargoes. J Cell Biol 160, 817–821.

Brown A (2014). Slow axonal transport. In: Reference Module in Biomedical Sciences, ed. M Caplan, Elsevier.

Brown A, Wang L, Jung P (2005). Stochastic simulation of neurofilament transport in axons: the "stop-and-go" hypothesis. Mol Biol Cell 16, 4243–4255.

Chakrabarty N (2020). Computational study of axonal transport mechanisms of actin and neurofilaments. PhD Thesis]. Athens, Ohio: Ohio University.

Chang R, Kwak Y, Gebremichael Y (2009). Structural properties of neurofilament sidearms: sequence-based modeling of neurofilament architecture. J Mol Biol 391, 648–660.

Ciocanel MV, Jung P, Brown A (2020). A mechanism for neurofilament transport acceleration through nodes of Ranvier. Mol Biol Cell 31, 640–654.

Cleveland DW, Monteiro MJ, Wong PC, Gill SR, Gearhart JD, Hoffman PN (1991). Involvement of neurofilaments in the radial growth of axons. J Cell Sci 1991 (Suppl 15), 85–95.

Costa AR, Pinto-Costa R, Sousa SC, Sousa MM (2018). The regulation of axon diameter: from axonal circumferential contractility to activity-dependent axon swelling. Front Mol Neurosci 11, 319.

Costa AR, Sousa MM (2021). The role of the membrane-associated periodic skeleton in axons. Cell Mol Life Sci 78, 5371–5379.

de Waegh SM, Lee VMY, Brad ST (1992). Local modulation of neurofilament phosphorylation, axonal caliber, and slow axonal transport by myelinating Schwann cells. Cell 68, 451–463.

Fenn JD, Johnson CM, Peng J, Jung P, Brown A (2018). Kymograph analysis with high temporal resolution reveals new features of neurofilament transport kinetics. Cytoskeleton (Hoboken) 75, 22–41.

Francis F, Roy S, Brady ST, Black MM (2005). Transport of neurofilaments in growing axons requires microtubules but not actin filaments. J Neurosci Res 79, 442–450.

Friede RL, Miyagishi T, Hu KH (1971). Axon calibre, neurofilaments, microtubules, sheath thickness and cholesterol in cat optic nerve fibres. J Anat 108(Pt 2), 365–373.

Friede RL, Samorajski T (1970). Axon caliber related to neurofilaments and microtubules in sciatic nerve fibers of rats and mice. Anat Rec 167, 379–387.

Garcia ML, Lobsiger CS, Shah SB, Deerinck TJ, Crum J, Young D, Ward CM, Crawford TO, Gotow T, Uchiyama Y, *et al*. (2003). NF-M is an essential target for the myelin-directed "outside-in" signaling cascade that mediates radial axonal growth. J Cell Biol 163, 1011–1020.

Hartline DK, Colman DR (2007). Rapid conduction and the evolution of giant axons and myelinated fibers. Curr Biol 17, R29–R35.

He J, Zhou R, Wu Z, Carrasco MA, Kurshan PT, Farley JE, Simon DJ, Wang G, Han B, Hao J, *et al*. (2016). Prevalent presence of periodic actin-spectrin-based membrane skeleton in a broad range of neuronal cell types and animal species. Proc Natl Acad Sci USA 113, 6029–6034.

He Y, Francis F, Myers KA, Yu W, Black MM, Baas PW (2005). Role of cytoplasmic dynein in the axonal transport of microtubules and neurofilaments. J Cell Biol 168, 697–703.

Hoffman PN (1995). The synthesis, axonal transport, and phosphorylation of neurofilaments determine axonal caliber in myelinated nerve fibers. Neuroscientist 1, 76–83.

Hoffman PN, Cleveland DW, Griffin JW, Landes PW, Cowan NJ, Price DL (1987). Neurofilament gene expression: a major determinant of axonal caliber. Proc Natl Acad Sci USA 84, 3472–3476.

Hoffman PN, Griffin JW, Gold BG, Price DL (1985a). Slowing of neurofilament transport and the radial growth of developing nerve fibers. J Neurosci 5, 2920–2929.

Hoffman PN, Griffin JW, Price DL (1984). Control of axonal caliber by neurofilament transport. J Cell Biol 99, 705–714.

Hoffman PN, Lasek RJ, Griffin JW, Price DL (1983). Slowing of the axonal transport of neurofilament proteins during development. J Neurosci 3, 1694–1700.

Hoffman PN, Thompson GW, Griffin JW, Price DL (1985b). Changes in neurofilament transport coincide temporally with alterations in the caliber of axons in regenerating motor fibers. J Cell Biol 101, 1332–1340.

Hsieh ST, Kidd GJ, Crawford TO, Xu Z, Lin WM, Trapp BD, Cleveland DW, Griffin JW (1994). Regional modulation of neurofilament organization by myelination in normal axons. J Neurosci 14, 6392–6401.

Jung P, Brown A (2009). Modeling the slowing of neurofilament transport along the mouse sciatic nerve. Phys Biol 6, 046002.

Lasek RJ, Oblinger MM, Drake PF (1983). Molecular biology of neuronal geometry: expression of neurofilament genes influences axonal diameter. Cold Spring Harb Symp Quant Biol 48, 731–744.

Lasek RJ, Paggi P, Katz MJ (1992). Slow axonal transport mechanisms move neurofilaments relentlessly in mouse optic axons. J Cell Biol 117, 607–616.

Leite SC, Sampaio PS, Vera F, Nogueira-Rodrigues J, Pinto-Costa R, Peters LL, Brites P, Sousa MM (2016). The actin-binding protein α-adducin is required for maintaining axon diameter. Cell Rep 15, 490–498.

Li Y, Jung P, Brown A (2012). Axonal transport of neurofilaments: a single population of intermittently moving polymers. J Neurosci 32, 746–758.

Malka-Gibor E, Kornreich M, Laser-Azogui A, Doron O, Zingerman-Koladko I, Harapin J, Medalia O, Beck R (2017). Phosphorylation-induced mechanical regulation of intrinsically disordered neurofilament proteins. Biophys J 112, 892–900.

Matthews MA, Duncan D (1971). A quantitative study of morphological changes accompanying the initiation and progress of myelin production in the dorsal funiculus of the rat spinal cord. J Comp Neurol 142, 1–22.

Monsma PC, Li Y, Fenn JD, Jung P, Brown A (2014). Local regulation of neurofilament transport by myelinating cells. J Neurosci 34, 2979–2988.

Mukhopadhyay R, Kumar S, Hoh JH (2004). Molecular mechanisms for organizing the neuronal cytoskeleton. Bioessays 26, 1017–1025.

Muma NA, Slunt HH, Hoffman PN (1991). Postnatal increases in neurofilament gene expression correlate with the radial growth of axons. J Neurocytol 20, 844–854.

Nixon RA, Logvinenko KB (1986). Multiple fates of newly synthesized neurofilament proteins: evidence for a stationary neurofilament network distributed nonuniformly along axons of retinal ganglion cell neurons. J Cell Biol 102, 647–659.

Nixon RA, Paskevich PA, Sihag RK, Thayer CY (1994). Phosphorylation on carboxyl terminus domains of neurofilament proteins in retinal ganglion cell neurons in vivo: influences on regional neurofilament accumulation, inter-neurofilament spacing, and axon caliber. J Cell Biol 126, 1031–1046.

Novak IL, Kraikivski P, Slepchenko BM (2009). Diffusion in cytoplasm: effects of excluded volume due to internal membranes and cytoskeletal structures. Biophys J 97, 758–767.

Perge JA, Niven JE, Mugnaini E, Balasubramanian V, Sterling P (2012). Why do axons differ in caliber? J Neurosci 32, 626–638.

Perrot R, Berges R, Bocquet A, Eyer J (2008). Review of the multiple aspects of neurofilament functions, and their possible contribution to neurodegeneration. Mol Neurobiol 38, 27–65.

Perrot R, Lonchampt P, Peterson AC, Eyer J (2007). Axonal neurofilaments control multiple fiber properties but do not influence structure or spacing of nodes of Ranvier. J Neurosci 27, 9573–9584.

Price RL, Paggi P, Lasek RJ, Katz MJ (1988). Neurofilaments are spaced randomly in the radial dimension of axons. J Neurocytol 17, 55–62.

Reles A, Friede RL (1991). Axonal cytoskeleton at the nodes of Ranvier. J Neurocytol 20, 450–458.

Sakaguchi T, Okada M, Kitamura T, Kawasaki K (1993). Reduced diameter and conduction velocity of myelinated fibers in the sciatic nerve of a neurofilament-deficient mutant quail. Neurosci Lett 153, 65–68.

Suminaite D, Lyons DA, Livesey MR (2019). Myelinated axon physiology and regulation of neural circuit function. Glia 67, 2050–2062.

Trivedi N, Jung P, Brown A (2007). Neurofilaments switch between distinct mobile and stationary states during their transport along axons. J Neurosci 27, 507–516.

Uchida A, Alami NH, Brown A (2009). Tight functional coupling of kinesin-1A and dynein motors in the bidirectional transport of neurofilaments. Mol Biol Cell 20, 4997–5006.

van Beijeren H, Kutner R (1985). Mean square displacement of a tracer particle in a hard-core lattice gas. Phys Rev Lett 55, 238–241.

Vejsada R, Palecek J, Hnik P, Soukup T (1985). Postnatal development of conduction velocity and fibre size in the rat tibial nerve. Int J Dev Neurosci 3, 583–595.

Walker CL, Uchida A, Li Y, Trivedi N, Fenn JD, Monsma PC, Lariviére RC, Julien JP, Jung P, Brown A (2019). Local acceleration of neurofilament transport at nodes of Ranvier. J Neurosci 39, 663–677.

Wang L, Ho CL, Sun D, Liem RK, Brown A (2000). Rapid movement of axonal neurofilaments interrupted by prolonged pauses. Nat Cell Biol 2, 137–141.

Watson DF, Hoffman PN, Fittro KP, Griffin JW (1989). Neurofilament and tubulin transport slows along the course of mature motor axons. Brain Res 477, 225–232.

Waxman SG (1980). Determinants of conduction velocity in myelinated nerve fibers. Muscle Nerve 3, 141–150.

Windebank AJ, Wood P, Bunge RP, Dyck PJ (1985). Myelination determines the caliber of dorsal root ganglion neurons in culture. J Neurosci 5, 1563–1569.

Xue C, Shtylla B, Brown A (2015). A stochastic multiscale model that explains the segregation of axonal microtubules and neurofilaments in neurological diseases. PLoS Comput Biol 11, e1004406.

Yuan A, Hassinger L, Rao MV, Julien JP, Miller CCJ, Nixon RA (2015). Dissociation of axonal neurofilament content from its transport rate. PLoS One 10, e0133848.

Yuan A, Rao MV, Veeranna NRA (2017). Neurofilaments and neurofilament proteins in health and disease. Cold Spring Harb Perspect Biol 9, a018309.

Yuan A, Sasaki T, Rao MV, Kumar A, Kanumuri V, Dunlop DS, Liem RK, Nixon RA (2009). Neurofilaments form a highly stable stationary cytoskeleton after reaching a critical level in axons. J Neurosci 29, 11316–11329.

Zhu Q, Couillard-Després S, Julien JP (1997). Delayed maturation of regenerating myelinated axons in mice lacking neurofilaments. Exp Neurol 148, 299–316.